Article

The Effect of Zinc Oxide Nanoparticles on Properties and Burn Wound Healing Activity of Thixotropic Xymedone Gels

Ilya Sheferov [1], Alyona Balakireva [2], Dmitry Panteleev [2], Irina Spitskaya [2], Sergey Orekhov [3], Oleg Kazantsev [3], Anna Solovyeva [4] (ID), Denis Novopoltsev [2] and Nina Melnikova [1,3,*] (ID)

[1] Faculty of Chemistry, Lobachevsky University, 603950 Nizhny Novgorod, Russia
[2] Department of Pharmacy, Privolzhsky Research Medical University, 603950 Nizhny Novgorod, Russia
[3] Research Laboratory "New Polymeric Materials", Nizhny Novgorod State Technical University n.a. R.E. Alekseev, 24 Minin St., 603950 Nizhny Novgorod, Russia
[4] Central Research Laboratory, Privolzhsky Research Medical University, 603950 Nizhny Novgorod, Russia
[*] Correspondence: melnikovanb@gmail.com; Tel.: +79-023-092298

Abstract: Zinc oxide nanoparticles (ZnO NPs) modified by oxopyrymidine alcohol, also known as xymedone (Xym), were obtained and studied using FTIR, UV-vis, and fluorescent spectroscopy, and SEM, BET, powder XRD, and DLS analysis. A formulation of thixotropic hydrophilic gels containing Carbopol-based Xym and ZnO NPs was developed. A vertical Franz cell with a cellulose acetate membrane was used as a model to investigate the passive diffusion of the gel components by AAS. The gel components—Xym and ZnO NPs—were shown to penetrate through acetyl cellulose membrane within 5–7 h depending on an initial amount, and its values were in the range of 56–77%. The penetration of modified ZnO NPs by Xym was more effective in contrast to ZnO NPs without modification. The burn wound healing activity of ZnO NPs–Xym gel was demonstrated on a thermal burn wound model on rats. SOD and GR activity was increased by 30–35% during ZnO NPs–Xym gel treatment, the burn area on 10 postburn day decreased by 10% in contrast to a positive control, Methyluracyl®® ointment.

Keywords: xymedone; ZnO nanoparticles; thixotropic gels; burn treatment; antioxidant activity; permeability

1. Introduction

Synthetic pyrimidine derivatives exhibiting pharmacological activity are of considerable interest in pharmacy and medicine. These compounds have low toxicity and are capable of increasing the immunobiological protective properties; stimulating hematopoiesis; exhibiting anti-inflammatory, antiviral, antitumor, antioxidant, membrane-stabilizing effects; and regulating tissue repair and regeneration [1–5].

The uracil or thymidine fragments of the ligand have all unique properties due to the N-heteroaromatic system necessary for selective action. Firstly, they are capable of stacking interactions with aromatic amino acid residues in enzymes (receptors) due to their aromatic system. Secondly, oxopyrymidines show a strong ability to hydrogen bond at the expense of oxygen atoms of carbonyl fragments or substituents in the pyrimidine cycle. Moreover, pyrimidine derivatives are similar in nature to pyridine nucleotides, which enables them to interact with some regions of protein molecules [2,6].

Xymedone (1-(β-oxyethyl)-4,6-dimethyl-1,2-dihydropyrimidin-2-one) is an interesting active pharmaceutical ingredient (API) with antioxidant, reparative, hepatoprotective, and anti-inflammatory activity [3]. The disadvantage of the substance to produce topical dosage forms is its high solubility depending on pH (94–285 g/L), which prevents effective penetration through both the intracellular and intercellular pathways and creation a dosage form with an optimal formulation. The high solubility and extremely low lipophilicity of xymedone are the reasons for its application in tablet dosage form only, despite the fact

that the effectiveness of xymedone topical dosage forms such as ointments, gels has been proven in experiments [3,7].

Recently, the substance's lipophilicity was shown to be regulated by the formation of complexes or conjugates with metals oxide nanoparticles [8,9]. As such, the conjugates of hydrophilic mildronate with nanoceria [10] and conjugates of methoxyoligo(ethylene glycol)methacrylate and betulin methacrylate with nanoceria [11] demonstrated a synergistic effect in a pharmacological activity.

Zinc oxide serving as a delivery vector for both hydrophilic and lipophilic substances in topical dosage forms [12–14] can be used for xymedone compositions. The most promising zinc oxide API are nanoparticles, which are small in size and, accordingly, have a large surface specific for xymedone immobilization. In addition, zinc oxide nanoparticles exhibit wound healing, anti-inflammatory, and bactericidal properties due to their ability to generate reactive oxygen species.

We previously showed that ZnO NPs demonstrate a synergistic effect with terpenes to prepare the gels enhancing their burn healing activity [15]. In particular, betulin diphosphate, betulin, and lavender oil components after immobilization onto ZnO NPs surface were shown both to enhance burn healing processes and to have antiaggregating and antiplatelet properties. Moreover, they improved a microhemicirculation in a burn wound.

To summarize, the ZnO NPs–xymedone conjugates can be considered as a promising API for inhibiting oxidative stress, increasing the cell metabolic status and wound healing.

In this work, we studied the immobilization of xymedone on the surface of zinc oxide nanoparticles (as a potential API), developed a topical thyxotropic dosage form of xymedone and zinc oxide nanoparticles, and studied the physicochemical and biological properties of the gels. The biological activity was studied using a thermal burn model in rats.

2. Materials and Methods

2.1. Materials

Xymedone (1-(β-hydroxyethyl)-4,6-dimethyl-1,2-dihydropyrimidin-2-one) (Xym), was purchased from the A. E. Arbuzova Institute Of Organic And Physical Chemistry (Kazan, Russia). Carbopol 974P NF (Lubrizol, Wycliff, Ohio, USA), ethanol (95.0% purity, Vekos, Nizhny Novgorod, Russia), zinc acetate dihydrate (99.0% purity, LenReaktiv, St. Petersburg, Russia), lithium hydroxide monohydrate (99.0% purity, CAS: 1310-66-3, Vekos, Nizhny Novgorod, Russia), polyethylene glycol (PEG 400) (Vekos, Nizhny Novgorod, Russia), cellulose acetate membrane (d = 0.45 μm, LenReaktiv, St. Petersburg, Russia), sodium chloride (99.9% purity, LenReaktiv, St. Petersburg, Russia), potassium phosphate trihydrate (99.0% purity, LenReaktiv, St. Petersburg, Russia), dipotassium phosphate trihydrate (99.0% purity, LenReaktiv, St. Petersburg, Russia), Methyluracyl$^{®®}$ as anointment (joint-stock company Nizhpharm, Nizhny Novgorod, Russia) were used in the study.

2.2. Synthesis of ZnO NPs

ZnO NPs were obtained by methods in accordance with work [16]. Briefly, a NaOH solution (10 mL, 2.0%) in ethanol (95.0%) was added to ethanolic $Zn(Ac)_2 \cdot 2H_2O$ solution (30 mL, 1.5%) cooled and stirred for 5–10 min. The resulting flocculent precipitate was precipitated with 60 mL of heptane, washed by ethanol and heptane, and dried (5 h at $105 \pm 5\,°C$).

2.3. Synthesis of PEGylated ZnO NPs

A total of 3.7 g of PEG 400 and 0.5 L of 0.175 M lithium hydroxide ethanol solution were added to 1.0 L of a freshly prepared 0.025 M zinc acetate ethanol solution under ultrasonic treatment (30 min). White ZnO particles were precipitated by adding cetyl alcohol (4.8 g) with stirring and the precipitate was washed with acetone and dried.

2.4. Gels Preparations

To obtain the gels, Carbopol 974 PNF was dispersed in purified water at room temperature while constantly stirring for 0.5–1 h. Xymedone solution and ZnO NP dispersion were prepared separately. The resulting mixtures were homogenized by ultrasound to obtain a homogeneous transparent rust-colored solution. Table 1 represents the composition of the studied gels.

Table 1. Formulation of investigated gels.

Gel	Composition, wt.%			
	Carbopol 974 PNF	**ZnO NPs**	**Xym**	**H$_2$O**
ZnO NPs	1.0	0.1	-	
ZnO NPs–Xym (5.0)	1.0	0.1	5.0	up to 100
ZnO NPs–Xym (2.5)	0.5	0.05	2.5	
Xym (5.0)	1.0	-	5.0	

2.5. FTIR Analysis

FTIR spectra were obtained in the 400–4000 cm^{-1} range by an IR Prestige-21 FTIR spectrometer (Shimadzu, Kyoto, Japan). The resolution was 0.5 cm^{-1}, and the number of scans was 45.

2.6. UV Analysis

UV spectra were obtained by UV-1800 spectrophotometer (Shimadzu, Kyoto, Japan).

2.7. Powder X-ray Diffraction Analysis

Powder X-ray diffraction patterns were recorded by Shimadzu X-ray diffractometer XRD-6000 (Shimadzu, Kyoto, Japan) at 295(2) K with Cu Kα radiation (λ = 0.15418 nm) using Bragg–Brentano reflection geometry.

The average powder size (D) was estimated using the Scherrer Equation (1) using the powder XRD pattern:

$$D = \frac{k\lambda}{\beta cos\theta} \tag{1}$$

where λ is the wavelength of the X-ray and equals 0.15056 nm, k is 0.89, β is a half-peak width of the diffraction peak, and θ is the Bragg angle.

2.8. Zinc Assay

Zinc assay was carried out by an atomic absorption spectrophotometer AA7000 (Shimadzu, Kyoto, Japan) at 213.9 nm. The samples were solved with HNO_3:$HClO_4$ (6:1) to obtain an ion form of zinc.

2.9. Photoluminescence Analysis

Fluorescent spectra were recorded using spectrofluorimeter RF-600 (Shimadzu, Kyoto, Japan) at the wavelength 320 nm in the field 350–800 nm in a quartz cuvette with 10 mm optical path.

2.10. Viscosity Estimation

Viscosity of dosage forms was measured using viscometer Brookfield DV2T with spindle 64 (AMETEK Brookfield, USA, Middleboro) equipped with a thermostat (Liquid low-temperature thermostat KRIO-VT-01; Termeks LLC, Tomsk, Russia) to maintain a temperature of 25 °C.

2.11. Surface Charge and Dynamic Light Scattering Measurements

The zeta potential and average hydrodynamic diameter of ZnO NPs were analyzed by NanoBrook Omni (Brookhaven Instruments, NY, USA) in a phosphate buffer solution at pH 7.4 after equilibration for 24 h. The Smoluchowski model was used to convert electrophoretic mobility values to zeta potential values. The hydrodynamic diameter of ZnO NPs was measured by dynamic light scattering (DLS) at 25 ± 0.1 °C at an angle of 90° in the range from 0.1 to 5000 nm in polystyrene cuvettes (1 cm). The accumulation time of the correlation function was 180 s ($n = 10$).

2.12. SEM and EDXMA Studies

The samples were visualized by scanning electron microscopy (SEM) on a JSM-IT300LV (JEOL, Tokyo, Japan) microscope with an electron beam diameter of about 5 nm and a probe current below 0.5 nA (operating voltage 20 kV). The surface topography of the powders was studied using low-energy secondary electrons and backscattered electrons. The elemental composition of the powders was studied using X-ray microprobe analysis (XRM) with an X-MaxN 20 detector (Oxford Instruments, Oxford, UK).

2.13. Specific Area Estimation

The specific surface area of powder materials was determined by static vacuum volumetry: a surface area analyzer, a micropore size, chemisorption "Autosorb iQ C" (Quantachrome Instruments, FL, USA). Before measurements, the samples were degassed under dynamic vacuum (base pressure = 1.33×10 Pa) at 120 °C for 3 h. The specific surface area of the powder was estimated with the Brunauer–Emmett–Teller (BET) method using the data taken in the range $0.05 < p/p_o < 0.35$.

2.14. Permeability Study

The permeability of xymedone and ZnO NPs was studied using a Franz cell (Figure S1) with acceptor chamber volumes of 4.35 mL and 12.65 mL, respectively. An acetyl cellulose membrane (d = 0.45 µm) with an area of 1.3 cm^2 was used as a model of stratum corneum.

2.15. Biological Activity

Male Wistar rats (250–300 g) were purchased from the Animal Breeding Facilities "Andreevka" Federal State Budgetary Institution of Science "Scientific Center for Biomedical Technologies", Federal Medical and Biological Agency (Andreevka, Moscow region, Russia). All procedures for maintenance and sacrifice (care and use) of animals were carried out according to the criteria outlined by European Convention ET/S 129, 1986 and directives 86/609 ESC. The animals were handled humanely, kept in plastic suspended cages, and placed in a well-ventilated and hygienic rat house under suitable conditions of a room temperature (27 ± 2 °C) and humidity. They were given food and water ad libitum and subjected to a natural photoperiod of 12 h light and 12 h dark cycle. The animals were allowed two weeks of acclimatization prior to the animal model experiments in the study.

All blood taking and withdrawal of experimental animals were performed under anesthesia (Zoletil 100 (60 mg/kg) and Xyl 6 mg/kg), and all effort was made to minimize suffering.

2.15.1. Modeling of Thermal Burns in Animals

The surface of the animals' backs were burned using electromagnetic radiation from an infrared soldering station YaXunXY865D according to the requirements of good laboratory practice for experimental modeling of thermal burns in laboratory animals. We used the regime causing thermal burns of second-degree depth. The distance of the infrared heater from the animal skin was 14.5 mm, the skin temperature in the heating zone was 60 °C, the heating duration was 23 s, and the power was 100 W. Under these conditions, infrared radiation penetrates to 3–5 mm deep [17,18]. The area of standard thermal burn was equal to 24.0 ± 0.5 cm^2, which was 20% off the total rat area.

2.15.2. Wound Area Measurement

The wound area was determined using a two-layered transparent film placed on the wound, and the outline was traced onto the film using a permanent marker.

After the measurement, the wound contraction was expressed as the percentage change compared to the original wound area using the following Formula (2) [19]:

$$Wound\ contraction = \frac{(Specific\ day\ wound\ area) \times 100\%}{(Original\ wound\ area)} \tag{2}$$

2.15.3. Biological Activity

Biochemical indexes were obtained using blood stabilized with sodium citrate on the 10th postburn day. Erythrocytes were washed twice with 0.9% NaCl by centrifugation for 10 min at $1600\times g$. Uchiyama and Mihara methods [20] were used to estimate the intensity of lipid peroxidation by the MDA level in plasma and erythrocytes. Superoxide dismutase activity (EC 1.15.1.1) was measured in erythrocytes using inhibition of adrenaline auto-oxidation [21]. Catalase activity (EC 1.11.1.6) was determined based on the decomposition of hydrogen peroxide by the catalase [22]. Glutathione reductase activity (EC 1.8.1.7) was studied by the oxidized glutathione reduction [23]. The catalytic activity of lactate dehydrogenase (EC 1.1.1.27) was studied in direct (LDH_{direct}, substrate, 50 mM sodium lactate) and reverse ($LDH_{reverse}$, substrate, 23 mM sodium pyruvate) reactions [24]. The modified Lowry method was used to assess the specific activity of the enzymes using the protein concentration [25]. The activity of aldehyde dehydrogenase (EC 1.2.1.3) was analyzed in accordance with previous methods [26].

2.15.4. Assessment of Microcirculation in Burn Wound

Microcirculation was studied quantitatively using the LAKK-02 (LASMA, Moscow, Russia). This device transmits continuous-wave laser light (30 mW, 890 nm) and white light (20 W, 500–900 nm) to skin tissue near the wound, where it is scattered and collected on the skin surface with probefibers. The movement of erythrocytes causes a Doppler shift, which in turn is detected by the laser light and analyzed by the LAKK-02 that is then computed and displayed as the blood flow velocity [27,28].

2.16. Statistical Analysis

Statistical data were processed by the software Statistica 6.0 (StatSoft Inc., Tulsa, OK, USA). The normality of results distribution was shown using the Shapiro–Wilks test. The significance of differences between groups was assessed using Student's *t*-test and one-way analysis of variance (ANOVA). The differences were considered statistically significant at $p < 0.05$.

3. Results and Discussion

3.1. Physicochemical Properties of Modified ZnO NPs

Figure 1 shows typical SEM images of the ZnO NPs obtained by sol-gel method (a), PEG-protected ZnO NPs (b), and ZnO NPs modified by xymedone (c). EDX spectrum and the element distribution of ZnO NPs–Xym powder on aluminum foil are shown in Figure 1d,e. These data characterized ZnO NPs–Xym powder as highly dispersed with a uniform distribution of elements throughout the powder volume. These results are in good agreement with the powder characteristics obtained by BET methods. Specific surface area of ZnO NPs–Xym was equal to 77.668 m^2/g, pore volume was 0.560 cm^3/g, and pore diameter Dv (d) was 1.111 nm.

The xymedone immobilization in the ZnO NPs surface was studied using UV-vis and FTIR spectra after xymedone treatment and washing with water and ethanol (Figure S2, Table 2).
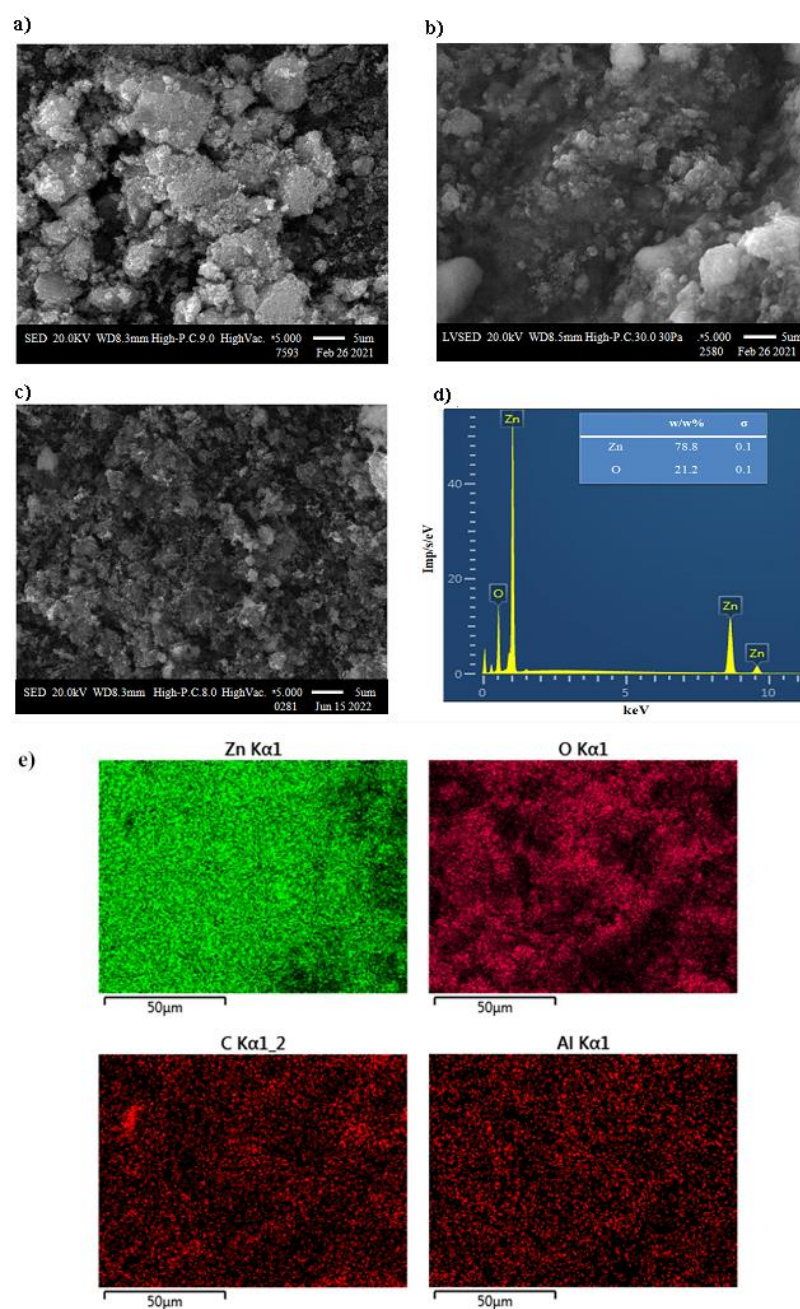
Figure 1. SEM images of ZnO NPs (**a**), ZnO NPs–PEG (**b**), ZnO NPs–Xym (**c**), EDX analysis of ZnO NPs–Xym (**d**,**e**). Analysis was carried out on aluminum foil.

Table 2. Comparison of FTIR spectra data for studied samples.

Substance	ν, cm^{-1}			
	3600–3200 (-OH, -NH and Other)	3100–2900 (-CH, -CH$_2$, -CH$_3$)	1655–1541 (-C=O, Amide I, Amide II)	470–450 (Zn-O in ZnO NPs)
ZnO NPs	3468	-	-	451
ZnO NPs–PEG	3375	-	-	453
ZnO NPs–Xym	3274	3100–2500	1544 1606 1659	452
Xymedone	3209	3100–2500	1541 1602 1655	-

The intense band of Zn-O stretching vibrations in the region of 451–453 cm^{-1} of FTIR spectra was observed for all studied samples (Figure S2). The FTIR spectrum of the solid xymedone powder in a KBr pellet (Figure S2d) has the bands of stretching vibrations of hydroxyl groups at 3397 and 3258 cm^{-1}, which is different from 3600 cm^{-1} characteristic of hydroxyl groups in the free state due to hydrogen bond effects. Other properties of the intermolecular hydrogen bond in the xymedone spectra are the bending band at 1410 cm^{-1}, and wagging vibrations of the adjacent CH$_2$ group, and a broad band at 676 cm^{-1} typical for torsional vibrations of the H-bonded OH group [6]. The spectrum (see Figure S2d) exhibits a strong band at 1653 cm^{-1} typical for the stretching vibration of the carbonyl group (ν(C=O)), two bands at 1064 and 1034 cm^{-1}. These frequency changes compared to the expected frequency for the free carbonyl group equal to 1700 cm^{-1} is related to intermolecular interactions. The presence of ZnO NPs–Xym bands characterized stretching vibrations of a carbonyl (C=O) group in the spectrum belonging to a pyrimidine lactam cycle in the regions of 1544–1541, 1606–1602, and 1659–1655 cm^{-1} was confirmed with xymedone immobilized into ZnO NPs.

Previously, xymedone was shown to be able to change its conformation depending on the biological conditions [6]. The "open" *gauche*-conformation of xymedone capable of intermolecular interaction by H-bonding determines its solubility in water and the possible transportation in aqueous media of the body. The "closed" xymedone gauche-conformation is more lipophilic and is able to penetrate through lipid layers of the cells.

The band wavelength in the surface plasmon resonance region of spectrum appeared at 352 nm in UV-vis spectra of all studied samples (Figure 2a). The nearly two-fold decrease in the absorption intensity of ZnO NPs–Xym compared to ZnO NPs at the same concentration characterizes the weakening of the surface plasmon resonance under the xymedone action.
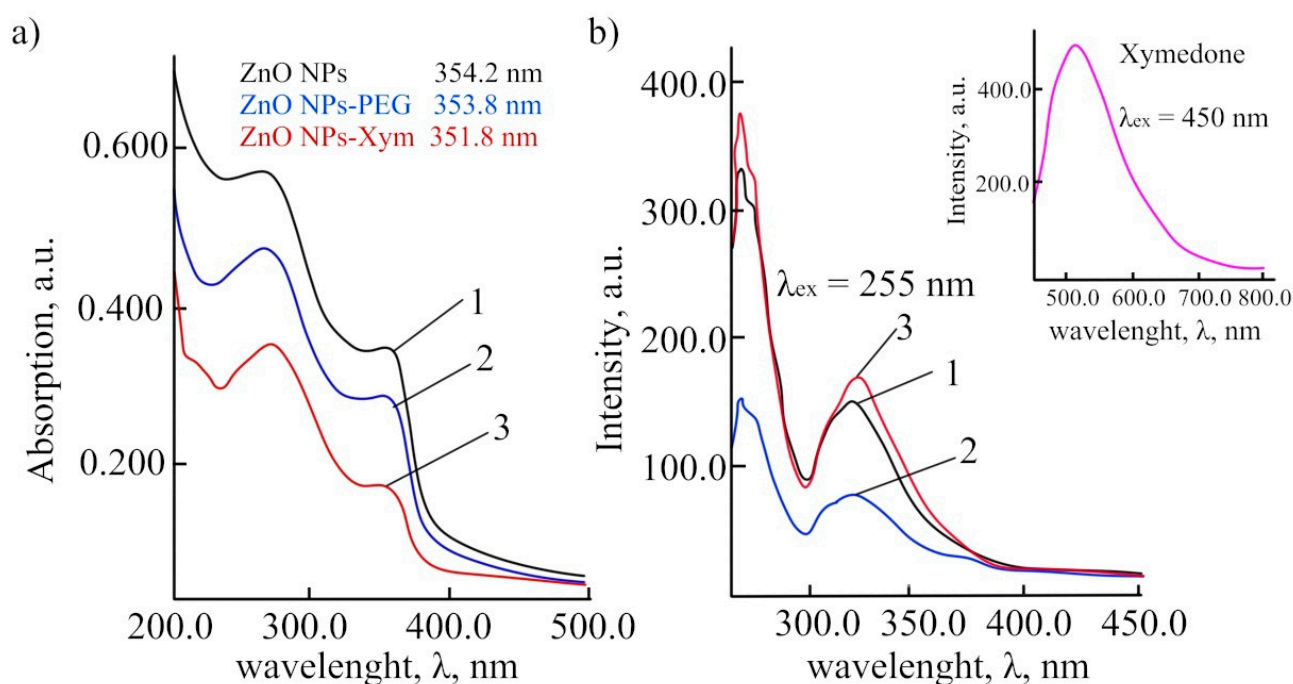

Figure 2. UV-vis (**a**) and fluorescence (**b**) spectra of ethanol dispersions of ZnO NPs of samples: ZnO NPs (curve 1); ZnO NPs–PEG (curve 2); ZnO NPs–Xym (curve 3). The insert shows fluorescence spectrum of xymedone.

Xymedone failed to desorb in aqueous and ethanol solutions. The fluorescence spectrum of ZnO NPs–Xym did not show a band typical for xymedone (Figure 2b). ZnO NPs–Xym demonstrated strong blue-violet emission at 276 nm with shoulder 280 nm, and exiton radiation appeared at 324 nm, such as ZnO NPs or ZnO NPs–PEG (Figure 2b).

The xymedone immobilization into the ZnO NPs surface was also confirmed by the PXRD data. We observed slight distortion of the Bragg angles in the diffraction patterns, which contained signals characteristic of both ZnO NPs and xymedone (Figure 3, Table S1). The xymedone diffraction patterns in ZnO NPs–Xym (Figure 3c) was close to the literature data [6].
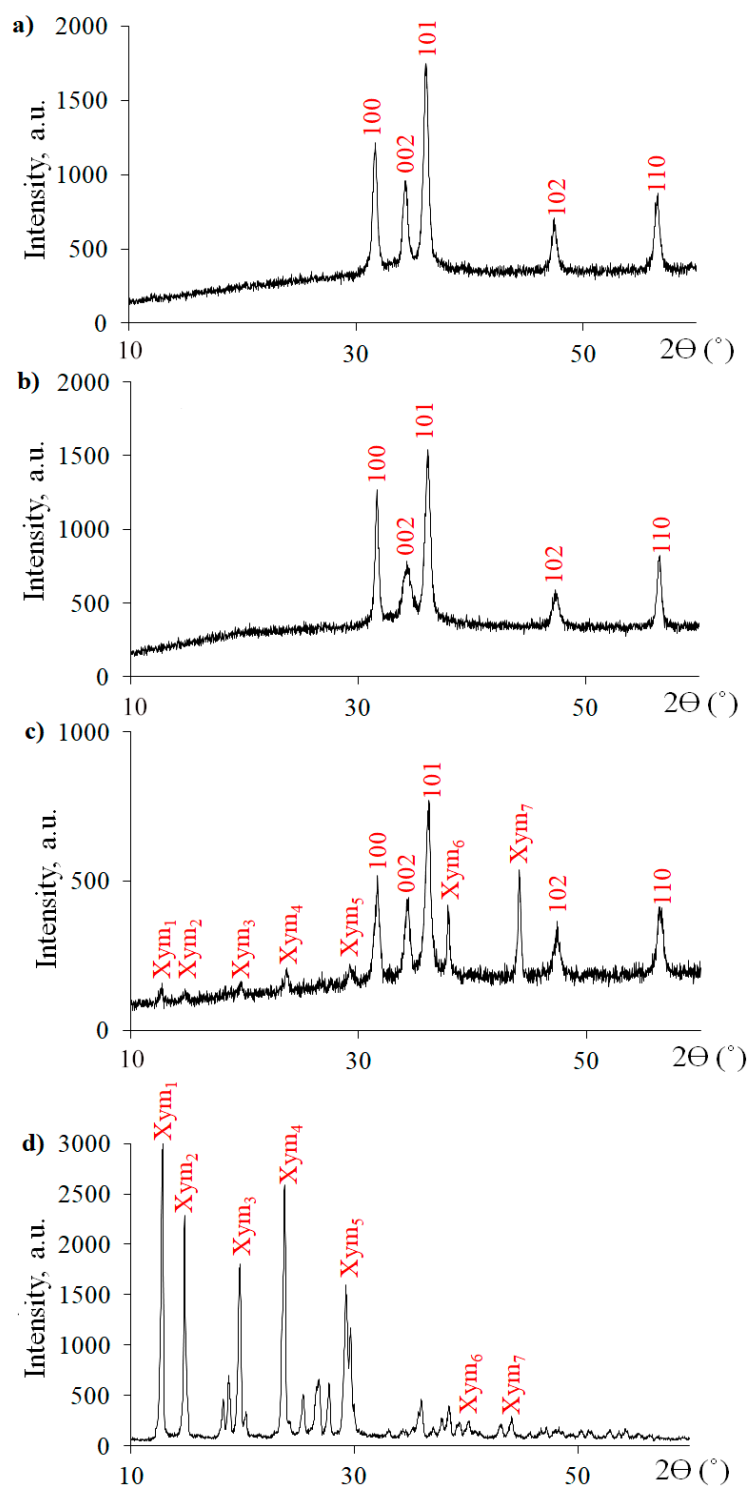

Figure 3. Powder XRD patterns of ZnO NPs (**a**), ZnO NPs–PEG (**b**), ZnO NPs–Xym (**c**), and xymedone (**d**).

The immobilization of ZnO NPs by xymedone is expected to result in a strong increase in hydrodynamic diameter in phosphate buffer saline. ZnO NPs stabilization in physiological conditions is very important. In fact, for the most part, one mode at 4500 nm was registered in the multimodal mode, but three out of ten measurements recorded the peaks at 100–200 nm (Figure 4a). One mode was also recorded with a maximum at 3700 nm (Figure 4b) at the weight and volume distribution. These findings characterize ZnO NPs–Xym as a stabilized API, which is suitable for hydrofilic dosage form preparation.
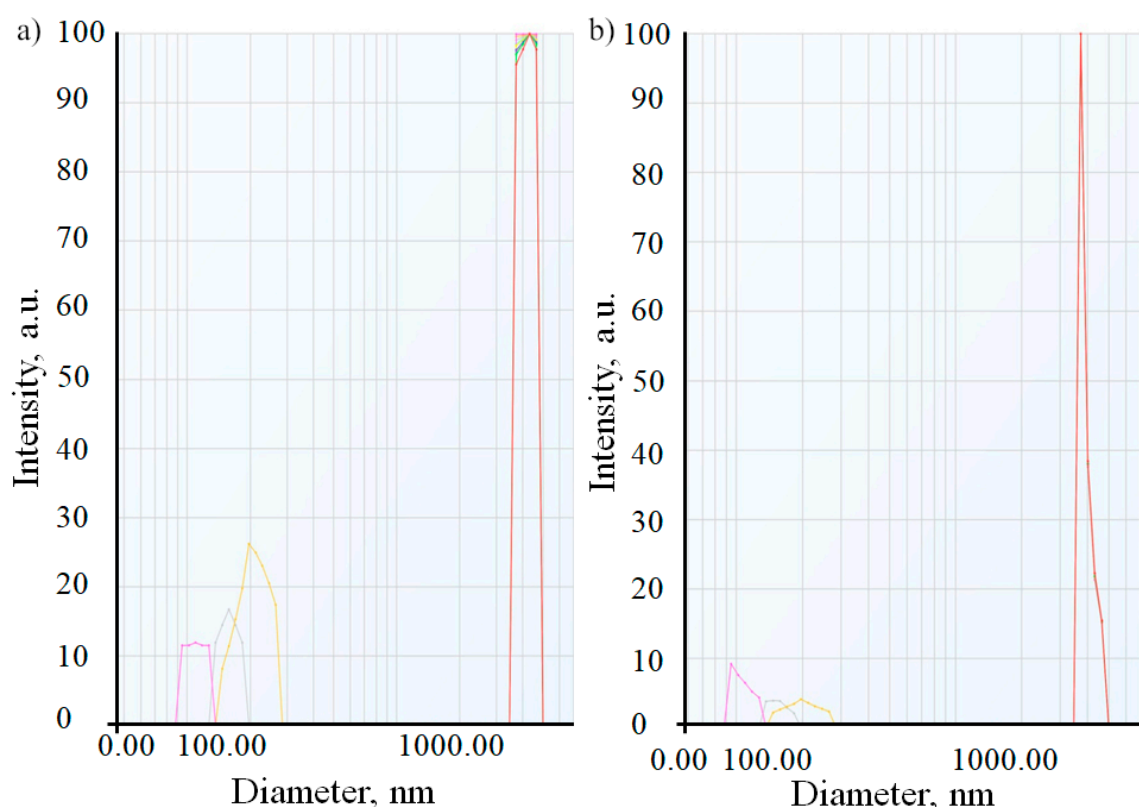

Figure 4. Particle size distribution for the ZnO NPs–Xym (**a**) sample by scattering intensity and (**b**) over the scattering volume (multimodal mode).

3.2. Rheological Properties of Gels

Rheological properties of Xym (5%) gel (Figure 5a) and ZnO NPs (0.05%)-Xym (2.5%) gel (Figure 5b) were studied based on the dependence of structural viscosity on the spindle speed, when studied the hysteresis loop in the compression and the stretch processes (Table 3).

The structural viscosity versus spindle speed in the direct and reverse states shows the small value of hysteresis loop, indicating the thixotropy of the studied gels (Table 3).

Table 3. Data of structural viscosity curves.

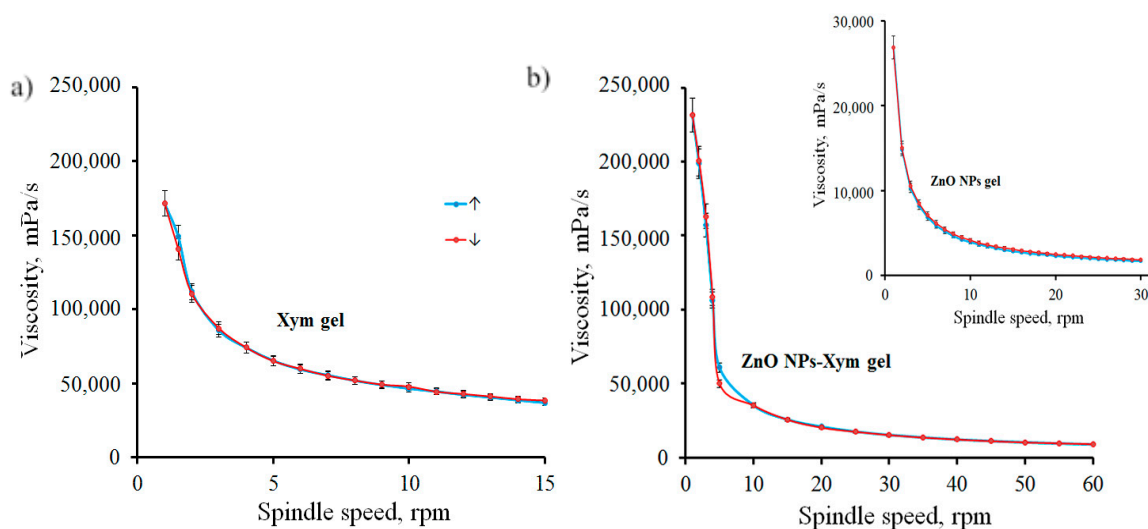| Samples	Area under Curve		Hysteresis Loop
	Compression	Stretch	
ZnO NPs (0.1%) gel	124,648	130,479	5831
ZnO NPs (0.05%)–Xym (2.5%) gel	260,957	262,261	1304
Xym (5%) gel	117,904	116,890	1014

Figure 5. Structural viscosity as a function of spindle speed for Xym (5%) gel (**a**) and ZnO NPs (0.05%)–Xym (2.5%) gel (**b**). The insert shows structural viscosity as a function of spindle speed for ZnO NPs (0.1%) gel. Blue lines correspond to compression and yellow-orange lines correspond to stretch.

The advantage of ZnO NPs (0.05%)–Xym (2.5%) gel was reaching an optimal structural viscosity required for thixotropic gels at a xymedone concentration that is two times lower compared to Xym (5%) gel.

The changes of ZnO NPs–Xym properties (IR, UV, fluorescence spectra, average hydrodynamic radius, and structural viscosity in gels) compared to those of the pure xymedone can be explained by the formation of various xymedone complexes with zinc ions on ZnO NPs surface at a physiological pH. Figure 6 illustrates possible structures of xymedone and its zinc complexes at various pH values.
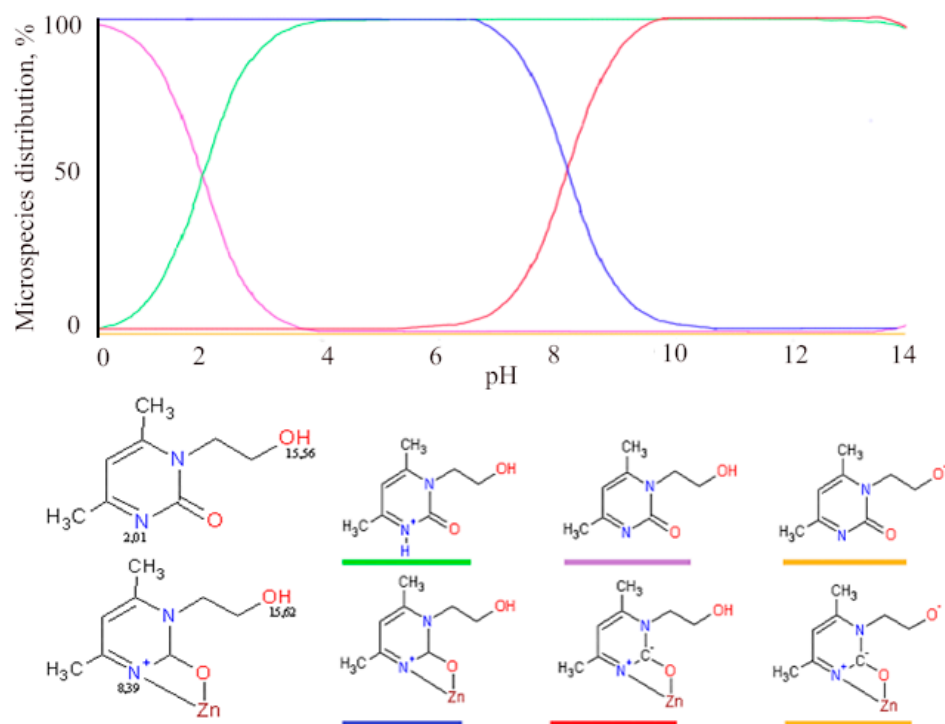

Figure 6. The dependence of microspecies distribution of xymedone and its zinc complexes (%) on pH.

According to Chemicalize calculations, the strong acid pKa for the alcohol xymedone group and its salt is equal to 15.58 ± 0.02, while the strong base pKa for the basic nitrogen is equal to 2.01 and 8.39 for the xymedone and its zinc salt, respectively. In general, lipophylity of ionizable complexes ZnO NPs–Xym should be higher than those of pure ZnO NPs or xymedone, but, however, zeta potential changes and increases. Table 4 presents the zeta potential values of ZnO NPs and ZnO NPs–Xym in PBS (pH 7.4). Zeta potential values depend not only on the modification of nanoparticles but also on a sample preparation. A period of 24 h after preliminary staying in PBS, the zeta potential of ZnO NPs–Xym increased by 36 mV and by 10 mV in comparison with ethanol:water medium and PBS, respectively.

Table 4. Zeta potential of 0.02% ZnO NPs dispersions at pH 7.4.

Sample	Medium	Zeta Potential, mV
ZnO NPs	Ethanol:water (1:1)	$+13.07 \pm 1.20$
ZnO NPs	PBS	-1.30 ± 1.11
ZnO NPs–Xym	PBS	-13.02 ± 2.79
ZnO NPs–Xym *	PBS	-23.79 ± 3.55

* Note: ZnO NPs–Xym were previously treated by PBS during 24 h.

3.3. Biomimetic Penetration of Xymedone and ZnO NPs–Xym from a 5% Gel through Theacetyl Cellulose Membrane

The permeability of ZnO NPs through the skin depends on a particle size, shape, surface charge, and surface functional groups. Generally, ZnO NPs should not penetrate the viable epidermis due to the natural barrier function of the layer. More lipophilic xymedone complex with Zn^{2+} than xymedone should have better penetration through the upper layer of the skin (stratum corneum, 200–400 μm) [13].

It is necessary to study biomimetically the dependence of ZnO NPs and Xym penetration into the wound through the stratum corneum on time to optimize the anti-burn gel formulation. Firstly, zinc oxide in topical dosage form fails to penetrate into the viable epidermis due to hydrolysis of ZnO and the increase of zinc ion content in the stratum corneum. Secondly, penetration depends on an animal skin type (rats, pigs, etc.). Moreover, the penetration depends on the interaction between all the components and skin.

We simulated the dynamics of components penetration on a model of acetyl cellulose membrane using a vertical Franz cell (Figure S1). Figure 7 shows the time dependence of the permeability of xymedone (Figure 7a,b) and zinc (Figure 7c) for the two gels—ZnO NPs (0.1%)–Xym (5%) gel and ZnO NPs (0.05%)–Xym (2.5%) gel.

The initial surface concentrations of xymedone in ZnO NPs (0.1%)–Xym (5%) gel and ZnO NPs (0.05%)–Xym (2.5%) gel on an acetyl cellulose membrane with an area of 1.3 cm^2 were 15,400 μg/cm^2 and 7700 μg/cm^2, respectively. The concentration values at the plateau (5–7 h) were in the range of $11,888 \pm 50$ μg/cm^2 and 4340 ± 35 μg/cm^2 for the concentrated and diluted gel, respectively, amounting to 77.2% and 56.3% of the initial concentrations. The permeability of zinc including soluble zinc ions and zinc oxide nanoparticles reached their maximum on the plateau in the same time interval (5–7 h)—36.5 ± 25 μg/cm^2, which is 58.6% of the initial total concentration (62.3 μg/cm^2).
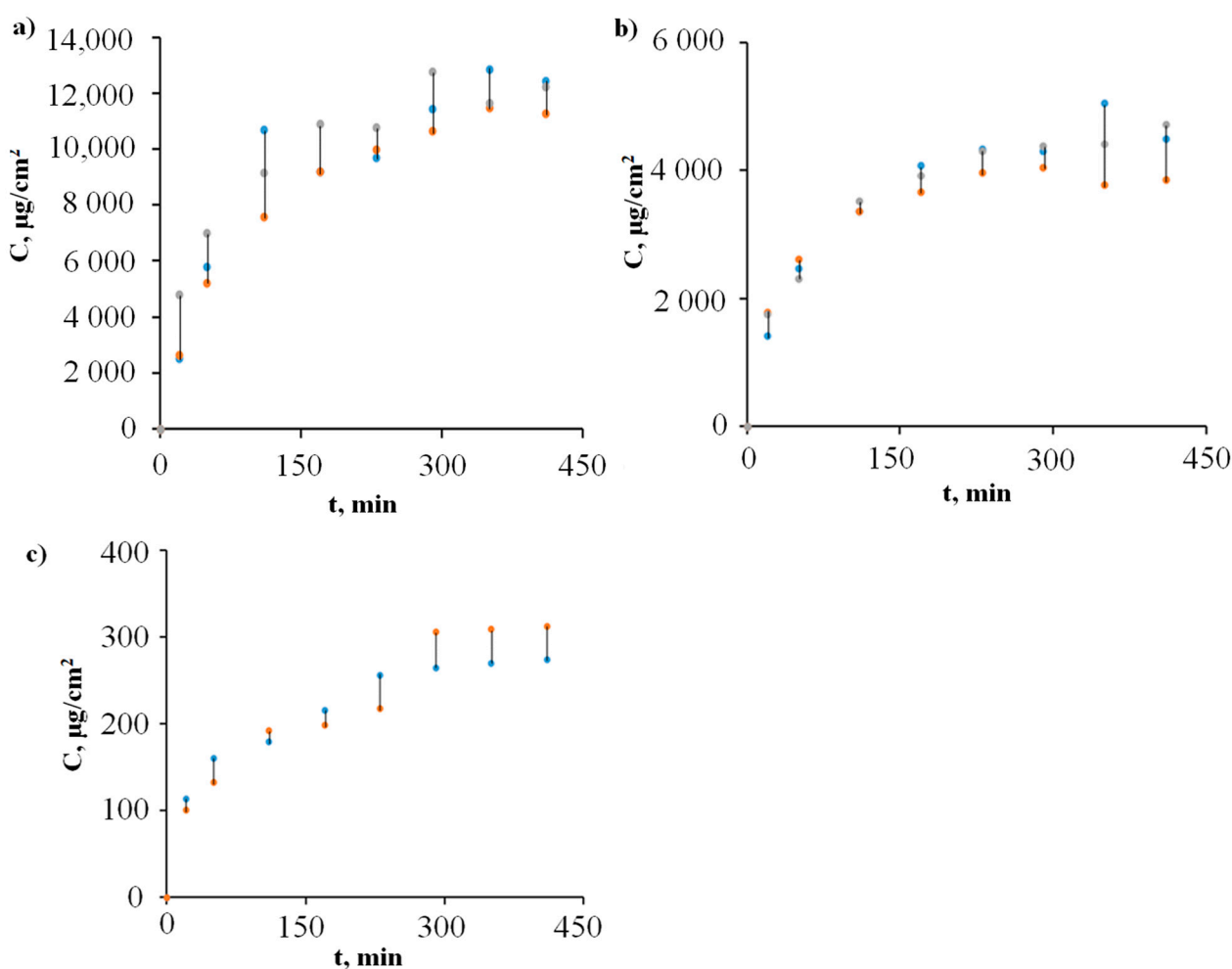
Figure 7. Dependence of xymedone permeability on the time through the acetyl cellulose membrane from ZnO NPs (0.1%)–Xym (5%) gel (**a**) and ZnO NPs (0.05%)–Xym (2.5%) gel (**b**). Dependence of Zn^{2+} permeability (C_{Zn}^{2+}, $\mu g/cm^2$) on time through the acetylcellulose membrane from ZnO NPs (0.05%)–Xym (2.5%) gel (**c**). Gel weight was equal to 400 mg onto membrane. The area under gel was equal to 1.3 cm^2.

3.4. Biological Activity of the Pharmaceutical Composition ZnO NPs–Xym Gel Using the Thermal Burn Wound Model

Figure 8 shows the visualization of the burn wounds during the treatment with Methyluracyl[®][®] (positive control) and ZnO NPs–Xym gel (experimental group). Figure S3 demonstrates a burn wound under treatment by ZnO NPs gel without xymedone (blank experiment).
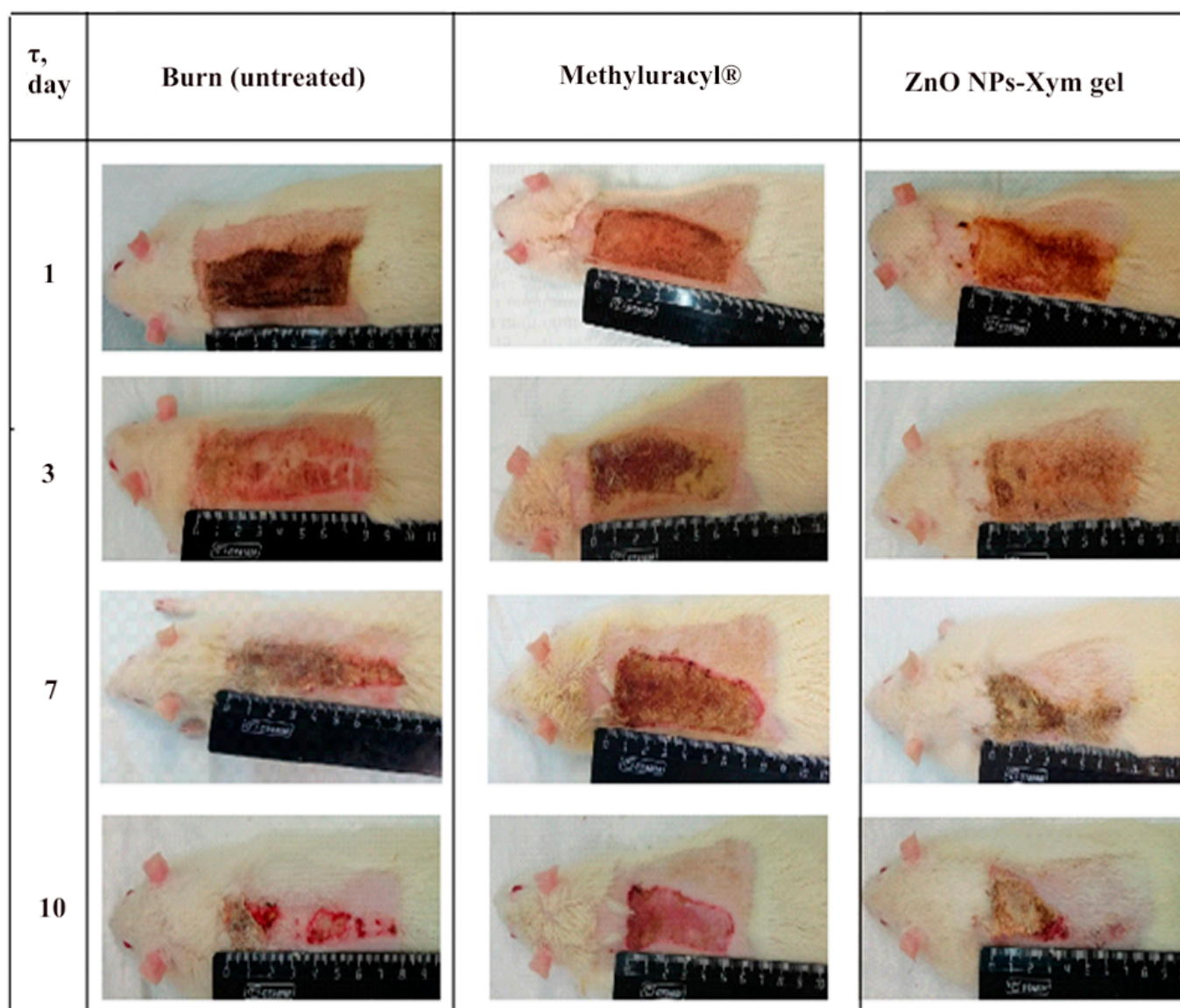
Figure 8. Photos of burn wound on rats under treatment with methyluracyl and ZnO NPs–Xym for 1, 3, 7, and 10 Days.

Table 5 shows the decrease in burn area under the treatment of Methyluracyl$^{®®}$, ZnO NPs gel and ZnO NPs–Xym gel. The decrease in burn area under the treatment of ZnO NPs–Xym gel (by 48%) was more significant than under the treatment of ZnO NPs gel (by 31%) and Methyluracyl ointment (by 40%).

Table 5. Change in wound area during treatment ($n = 3$, $p < 0.05$).

Group	Burn Area			
	0 Day		10 Day	
	cm^2	% of Control	cm^2	% of Control
Burn untreated (negative control)	23.97 ± 0.54	100	18.48 ± 0.35	77
Methyluracyl$^{®®}$ (positive control)	25.03 ± 0.48	100	15.01 ± 0.39	60
ZnO NPs–Xym gel	24.45 ± 0.25	100	12.75 ± 0.54	52
ZnO NPs gel	24.67 ± 0.23	100	16.94 ± 0.27	69

The burn wound state was assessed by microcirculation intensity by laser Doppler flowmetry (LDF) [28]. We calculated the oscillations with different amplitudes characterizing the endothelial (E), myogenic (M), and neurogenic (N) frequency regions of the LDF spectra, which determine the contribution of regulation mechanisms of the lumen of blood vessels and their tone. LDF spectra data enable for the estimation of the erythrocyte rate and tissue oxygenation in the blood flow (perfusion).

Using the average amplitude of the reflected signal in the microhemicirculatory flow, we obtained the average Doppler frequency shift over all the probed areas. Typical amplitude–frequency spectra after the wavelet transform are presented in Figure S4 [29].

The results of the LDF spectra are presented in arbitrary units (perfusion units) as a microcirculation indicator (MI). Table 6 shows the dynamics of perfusion change on the burn (day 0) and under the treatment on day 10 after burn as different indexes calculated by neurogenic (N), myogenic (M), cardiac (C), endothelial (E), and respiratory bands in wavelet spectra. On day 10 after the burn and under treatment, the respiratory and cardiac bands of wavelet spectra (oxygenation of the microvasculature tissue) approached those of the intact rats. At the same time, all other LDF signals decreased.

Table 6. The microhemicirculatory indexes calculated by laser Doppler flowmetry for intact rats, untreated burnt rats (day 0), and burnt rats (day 10) under the treatment by ZnO NPs–Xym gel, ZnO NPs gel, and Methyluracyl[®®] ointment $n = 3$, $p < 0.05$.

Group	MI, perf. un	E, arb. un	N, arb. un	M, arb. un	R, arb. un	C, arb.un
Intact	9.45 ± 0.85	12.93 ± 1.15	9.15 ± 0.86	8.37 ± 0.81	5.80 ± 0.49	3.33 ± 0.27
Burn nontreatment (negative control)	12.18 ± 1.11	14.04 ± 1.28	13.84 ± 1.26	15.34 ± 1.40	16.42 ± 1.49	9.50 ± 0.86
Methyluracyl[®®] (positive control)	10.36 ± 0.94	11.89 ± 1.08	11.94 ± 1.09	10.93 ± 0.99	10.87 ± 0.99	7.62 ± 0.69
ZnO NPs–Xym gel	9.40 ± 0.85	12.83 ± 1.17	10.73 ± 0.98	6.94 ± 0.63	7.34 ± 0.67	4.83 ± 0.44
ZnO NPs gel	10.01 ± 0.45	11.07 ± 0.98	12.13 ± 0.56	11.56 ± 0.98	12.49 ± 0.56	7.23 ± 0.72

Note: perf. un.: perfusion units, arb. un.: arbitrage units, E: endothelial, N: neurogenic, M: myogenic, R: respiratory and C: cardiac oscillations.

In general, the normalization of the microhemicirculatory indexes suggesting blood flow regulation and oxygenation in a burnt zone, on day 10 was more effective under the treatment by ZnO NPs–Xym gel than by Methyluracyl[®®] (positive control) and by ZnO NPs gel.

The tissue oxygenation in the blood flow (perfusion) was associated with an enzymes activity that provides cellular respiration in erythrocytes.

Table 7 presents the data on the specific activity assessment of lactate dehydrogenase (LDH) in direct and reverse reactions on rat blood on day 10 under treatment with Methyluracyl[®®], ZnO NPs gel and ZnO NPs–Xym gel. The specific activity of LDH_{dir} under the action of ZnO NPs–Xym gel was 22% and 31% higher than that of LDH_{dir} under the treatment by Methyluracyl[®®] and ZnO NPs gel, respectively. In contrast, LDH_{rev} specific activity decreased by 43% and by 34% when rats were treated by ZnO NPs–Xym gel in comparison with Methyluracyl[®®] and ZnO NPs gel. The results suggest the ZnO NPs–Xym gel provides more gentle cellular respiration and energy metabolism, since it contributes more to pyruvate production, which is necessary for the Krebs cycle.

Table 7. Specific activity of AlDH and LDH in direct and reverse reactions, and the MDA level on the rat blood on the 10th day after thermal burn under the treatment by dosage forms, in % of control ($n = 3$, $p < 0.05$).

Group	Biochemical Indexes, % of Control			
	LDH_{direct}	$LDH_{reverse}$	**AlDH**	MDA_{er}
Burn untreated (negative control)	100.0	100.0	100.0	100.0
Methyluracyl[®®] (positive control)	122.47	142.58	125.75	105.89
ZnO NPs–Xym gel	142.02	99.32	124.04	102.21
ZnO NPs gel	111.52	135.29	110.93	115.35

Note: mean values for LDH_{direct}, $LDH_{reverse}$, AlDH, and MDA in burn untreated group were equal to 38.329 ± 1.398 nmol NAD + /min·mg protein; 172.882 ± 5.198 nmol NADH/min·mg protein; 44.323 ± 2.09 nmol NADH/min·mg protein, 7.577 ± 0.324 μmol/L, respectively, taken as 100%.

This plasticity in the regulation of metabolic processes is essential under the conditions of hypoxia in a burn injury.

The AlDH activity, which is involved in oxidative stress reduction, including the utilization of MDA in erythrocytes, increased by 24–25% under the treatment by Methyluracyl[®®] and ZnO NPs–Xym gel, and by 10% under the ZnO NPs gel treatment (Table 7). The MDA level in erythrocytes did not change significantly in the cases of Methyluracyl and ZnO NPs–Xym gel treatment and remained close to AlDH activity in the "Burn untreated" group, but MDA_{er} level increased by 15%.

The activation of specific antioxidant enzymes such as SOD, catalase and GR, was observed in the positive control (Methyluracyl[®®] ointment), the ZnO NPs gel group, and the experimental group (ZnO NPs–Xym gel) (Table 8).

Table 8. Specific activity of SOD, catalase, and GR on the rat blood on the 10th day after thermal burn under the treatment by dosage forms, in % of control ($n = 3$, $p < 0.05$).

Group	Biochemical Indexes, % of Control		
	SOD	**Catalase**	**GR**
Burn untreated (negative control)	100.0	100.0	100.0
Methyluracyl[®®] (positive control)	130.78	105.16	183.44
ZnO NPs–Xym gel	135.02	104.50	160.26
ZnO NPs gel	110.28	98.39	120.98

Note: mean values for SOD, catalase, GR in burn untreated group were equal to 917.366 ± 23.545 a.u./min·mg protein; 33.282 ± 1.125 μmol H_2O_2/min·mg protein; 72.384 ± 5.983 NADPH/min·mg protein, respectively, taken as 100%.

At the same time, the differences in the specific activity of SOD and catalase were insignificant, and GR activity increased more intensively for methyluracil ointment (by 83%) compared to ZnO NPs–Xym gel (by 60%). Consequently, glutathione, a strong antioxidant, is formed more under the action of methyluracil ointment, which indirectly characterizes the stronger antioxidant properties of methyluracil compared to the proposed pharmaceutical composition. This effect can probably be explained by the competitive generation of reactive oxygen species under the action of ZnO NPs. However, the presence of ZnO NPs only did not provide such effects (Table 8).

The microhemicirculation data, antioxidant properties, and wound healing data under the action of ZnO NPs–Xym gel show a synergistic effect due to xymedone, ZnO NPs, and conjugates of xymedone with ZnO NPs. Surface ZnO NPs–Xym complexes were proven by FTIR spectral data, PXRD patterns, and the changes of zeta potential values after xymedone immobilization. ZnO NPs–Xym complexes improve the dynamics of the release of components from the dosage form in contrast to ZnO NPs without modification. Moreover, the formation of ZnO NPs–Xym conjugates allows for the design of stable thixotropic gels based on hydrophilic polyacrilic acid using small concentration of xymedone and ZnO NPs.

4. Conclusions

Thus, zinc oxide nanoparticles modified by xymedone ZnO NPs–Xym can be proposed as a potential API to develop new dosage forms of xymedone for burn treatment. Although in this work we demonstrated a thermal wound healing effect, the pharmaceutical composition with ZnO NPs–Xym can also be used to treat burns of other tissues. The advantage of the developed formulation of ZnO NPs–Xym gel is a high thixotropy of the composition, which enables not only a reduction in the xymedone concentration by 2–3 times, but also ensures the necessary permeability of the components through the corneum stratum. Moreover, the gel thixotropy can be used to create new oral dosage forms to treat the burns of the gastrointestinal mucosa.

Supplementary Materials: The following supporting information can be downloaded at: https://www.mdpi.com/article/10.3390/scipharm90040061/s1, Figure S1: Schematic design of vertical Franz diffusion cell. Cell volume was equal to 12.65 mL and 4.35 mL for analysis of ZnO NPs and Xym, respectively; Figure S2: FTIR spectra of ZnO NPs (a), ZnO NPs–PEG (b), ZnO NPs–Xym (c), and xymedone (d); Table S1: Data of powder XRD patterns of ZnO NPs, ZnO NPs–PEG, ZnO NPs–Xym, and xymedone; Figure S3: Photos of burn wound on rats under the treatment by ZnO NPs gel for 3, 7, and 10 days; Figure S4: Wavelet–LDF spectra (amplitude = f(frequency)) obtained by laser Doppler flowmetry for intact rats (a), untreated burnt rats (day 0, b), burnt rats (day 10) under the treatment by ZnO NPs–Xym gel (c), and Methyluracyl®® ointment (d). Neurogenic (N), myogenic (M), cardiac (C), endothelial (E), and respiratory (R) bands are presented on spectra.

Author Contributions: N.M. conceived and designed the experiments, analyzed the data, and wrote the paper; A.S. and D.N. performed biochemical experiments, S.O., O.K. and D.P. performed physicochemical experiments; A.B. and I.S. (Ilya Sheferov), I.S. (Irina Spitskaya) obtained substances and gel-like dispersions. All authors have read and agreed to the published version of the manuscript.

Institutional Review Board Statement: The study was conducted in accordance with the Declaration of Helsinki and approved by the Local Ethics Committee of Privolzhsky Research Medical University, Russian Federation (protocol No. 1 on 18 January 2021; protocol No. 2 on 20 February 2016).

Informed Consent Statement: Informed consent was obtained from all subjects involved in the study.

Data Availability Statement: The data presented in this study are available upon reasonable request from the corresponding author.

Conflicts of Interest: The authors declare no conflict of interest.

References

1. Bano, T.; Kumar, N.; Dudhe, R. Free radical scavenging properties of pyrimidine derivatives. *Org. Med. Chem. Lett.* **2012**, *14*, 34. [CrossRef]
2. He, Z.-X.; Zhao, T.-Q.; Gong, Y.-P.; Zhang, X.; Ma, L.-Y.; Liu, H.-M. Pyrimidine: A promising scaffold for optimization to develop the inhibitors of ABC transporters. *Eur. J. Med. Chem.* **2020**, *200*, 112458. [CrossRef]
3. Izmailov, S.G.; Izmailov, G.A.; Averyanov, M.Y.; Reznik, V.S. *Xymedon in Clinical Practice*, 1st ed.; NNSMA: Nizhny Novgorod, Russia, 2001; p. 185. ISBN 5-7032-0112-8.
4. Pradere, U.; Garnier-Amblard, E.C.; Coats, S.J.; Amblard, F.; Schinazi, R.F. Synthesis of nucleoside phosphate and phosphonate prodrugs. *Chem. Rev.* **2014**, *114*, 9154–9218. [CrossRef]
5. Zhang, Y.; Geng, H.; Junjie, Z.; He, K. An update mini-review on the progress of azanucleoside analogues. *Chem. Pharm. Bull.* **2022**, *70*, 469–476. [CrossRef] [PubMed]
6. Zvereva, E.E.; Vandyukova, I.I.; Vandyukov, A.E.; Katsyuba, S.A.; Khamatgalimov, A.R.; Kovalenko, V.I. IR and Raman spectra, hydrogen bonds, and conformations of N-(2-hydroxyethyl)-4,6-dimethyl-2-oxo-1,2-dihydropyrimidine (drug Xymedone). *Russ. Chem. Bull. Int. Ed.* **2012**, *61*, 1199–1206. [CrossRef]

7. Beschastnov, V.V.; Izmailov, S.G.; Botyakov, A.A.; Zharinov, A.Y.; Panteleev, D.A.; Melnikova, N.B. Antioxidant activity of pyrimidine derivatives in the local treatment of purulent wounds of soft tissues (in experiment). *Mod. Technol. Med.* **2011**, *3*, 21–26. (In Russian)

8. Krysanov, E.; Demidova, T.; Ivanova, O.; Ordzhonikidze, K.; Shcherbakov, A.; Ivanov, V. Synergetic action of ceria nanoparticles and doxorubicin on the early development of two fish species, Danio rerio and Puntius tetrazona. *Nanosyst. Phys. Chem. Math.* **2019**, *10*, 289–302. [CrossRef]

9. Sack, M.; Alili, L.; Karaman, E.; Das, S.; Gupta, A.; Seal, S.; Brenneisen, P. Combination of Conventional Chemotherapeutics with Redox-Active Cerium Oxide Nanoparticles—A Novel Aspect in Cancer Therapy. *Mol. Cancer Ther.* **2014**, *13*, 1740–1749. [CrossRef]

10. Popov, A.L.; Kolmanovich, D.D.; Popova, N.R.; Sorokina, S.S.; Ivanova, O.S.; Chukavin, N.N.; Shcherbakov, A.B.; Kozlova, T.O.; Kalashnikova, S.A.; Ivanov, V.K. Synthesis and biocompatibility study of ceria-mildronate nanocomposite in vitro. *Nanosyst. Phys. Chem. Math.* **2022**, *13*, 96–103. [CrossRef]

11. Melnikova, N.; Orekhov, D.; Simagin, A.; Malygina, D.; Korokin, V.; Kosmachova, K.; Al-Azzavi, H.; Solovyeva, A.; Kazantsev, O. Antioxidant Activity of New Copolymer Conjugates of Methoxyoligo(Ethylene Glycol)Methacrylate and Betulin Methacrylate with Cerium Oxide Nanoparticles In Vitro. *Molecules* **2022**, *27*, 5894. [CrossRef]

12. Gupta, M.; Mahajan, V.K.; Mehta, K.S.; Chauhan, P.S. Zinc Therapy in Dermatology: A Review. *Dermatol. Res. Pract.* **2014**, *2014*, 709152. [CrossRef] [PubMed]

13. Holmes, A.M.; Song, Z.; Moghimi, H.R.; Roberts, M.S. Relative Penetration of Zinc Oxide and Zinc Ions into Human Skin after Application of Different Zinc Oxide Formulations. *ACS Nano* **2016**, *10*, 1810–1819. [CrossRef] [PubMed]

14. Negut, I.; Grumezescu, V.; Grumezescu, A.M. Treatment Strategies for Infected Wounds. *Molecules* **2018**, *23*, 2392. [CrossRef]

15. Melnikova, N.; Balakireva, A.; Orekhov, D.; Kamorin, D.; Didenko, N.; Malygina, D.; Knyazev, A.; Novopoltsev, D.; Solovyeva, A. Zinc Oxide Nanoparticles Protected with Terpenoids as a Substance in Redox Imbalance Normalization in Burns. *Pharmaceuticals* **2021**, *14*, 492. [CrossRef] [PubMed]

16. Bera, D.; Qian, L.; Sabui, S.; Santra, A.; Holloway, P.H. Photoluminescence of ZnO quantum dots produced by a sol-gel process. *Opt. Mater.* **2008**, *30*, 1233–1239. [CrossRef]

17. Pakhomova, A.E.; Pakhomova, E.E.; Pakhomova, J.V.; Yavorsky, E.M. Method Experimental Modeling of Thermal Combustion at Laboratory Animals. Patent No. RU 2,582,458 C1, 24 December 2014.

18. Pakhomova, A.E.; Pakhomova, J.V.; Ovsyanko, E.V.; Zhurakovsky, I.P.; Karabintseva, N.O.; Pakhomova, E.E. Preclinical research of repalen ointment at treatment of thermal combustions in experiment. *J. Sib. Med. Sci.* **2015**, *3*, 98.

19. Hosseinimehr, S.J.; Khorasani, G.; Azadbakht, M.; Zamani, P.; Ghasemi, M.; Ahmadi, A. Effect of aloe cream versus silver sulfadiazine for healing burn wounds in rats. *Acta. Dermatovenerol. Croat.* **2010**, *18*, 2–7.

20. Mihara, M.; Uchiyama, M. Determination of malonaldehyde precursor in tissues by thiobarbituric acid test. *Anal. Biochem.* **1978**, *86*, 271–278. [PubMed]

21. Sirota, T.V. A new approach to studying the autoxidation of adrenaline: Possibility of the determinationof superoxide dismutase activity and the antioxidant properties of various preparations by polarography. *Biomed. Khi.* **2012**, *58*, 77–87. [CrossRef]

22. Packer, L. Catalase in Vitro. In *Methods in Enzymology*; Academic Press: Cambridge, MA, USA, 1984; Volume 105, pp. 121–126.

23. Sibgatullina, G.V.; Khartendinova, L.R.; Gumerova, E.A.; Akulov, A.N.; Kostyukova, Y.A.; Nikonorova, N.A.; Rumyantseva, N.I. *Methods for Determining the Redox Status of Cultured Plant Cells*, 1st ed.; Kazan Federal University: Kazan, Russia, 2011; pp. 18–20.

24. Solovyeva, A.G.; Zimin, Y.V. A new way to assess the dynamics of blood metabolism in patients with thermal trauma. *Mod. Technol. Med.* **2012**, *2*, 116–117.

25. Dawson, J.M.; Heatlic, P.L. Lowry method of protein quantification evidence for photosensitivity. *Anal. Biochem.* **1984**, *140*, 391–393. [CrossRef]

26. Guru, S.C.; Shetty, K.T. Methodological aspects of aldehyde dehydrogenase assay by spectrophotometric technique. *Alcohol* **1990**, *7*, 397–401. [CrossRef]

27. Dahmus, J.D.; Bruning, R.S.; Kenney, W.L.; Alexander, L.M. Oral clopidogrel improves cutaneuos microvascular function through EDHF-dependent mechanisms in middle-aged humans. *Am. J. Physiol. Regul. Integr. Comp. Physiol.* **2013**, *305*, R452–R458. [CrossRef] [PubMed]

28. Krupatkin, A.I.; Sidorov, V.V. *Functional Diagnostics of the State of Microcirculatory-Tissue Systems: Oscillations, Information, Nonlinearity: A Guide for Physicians*, 1st ed.; Librokom: Moscow, Russia, 2013; p. 496.

29. Stefanovska, A.; Bracic, M.; Desiree Kvernmo, H. Wavelet Analysis of Oscillations in the Peripheral Blood Circulation Measured by Laser Doppler Technique. *IEEE Trans. Biomed. Eng.* **1999**, *46*, 1230–1239. [CrossRef]